SAND REPORT

SAND2003-0668
Unlimited Release
Printed March 2003

GaAs MOEMS Technology

Olga Spahn, Grant Grossetete, Mike Cich, Chris Tigges,
John Reno, Greg Peake, John Klem

Approved for public release; further dissemination unlimited.

🔲 Sandia National Laboratories

Issued by Sandia National Laboratories, operated for the United States Department of Energy by Sandia Corporation.

NOTICE: This report was prepared as an account of work sponsored by an agency of the United States Government. Neither the United States Government, nor any agency thereof, nor any of their employees, nor any of their contractors, subcontractors, or their employees, make any warranty, express or implied, or assume any legal liability or responsibility for the accuracy, completeness, or usefulness of any information, apparatus, product, or process disclosed, or represent that its use would not infringe privately owned rights. Reference herein to any specific commercial product, process, or service by trade name, trademark, manufacturer, or otherwise, does not necessarily constitute or imply its endorsement, recommendation, or favoring by the United States Government, any agency thereof, or any of their contractors or subcontractors. The views and opinions expressed herein do not necessarily state or reflect those of the United States Government, any agency thereof, or any of their contractors.

Printed in the United States of America. This report has been reproduced directly from the best available copy.

Available to DOE and DOE contractors from
    U.S. Department of Energy
    Office of Scientific and Technical Information
    P.O. Box 62
    Oak Ridge, TN 37831

    Telephone: (865)576-8401
    Facsimile: (865)576-5728
    E-Mail: reports@adonis.osti.gov
    Online ordering: http://www.doe.gov/bridge

Available to the public from
    U.S. Department of Commerce
    National Technical Information Service
    5285 Port Royal Rd
    Springfield, VA 22161

    Telephone: (800)553-6847
    Facsimile: (703)605-6900
    E-Mail: orders@ntis.fedworld.gov
    Online order: http://www.ntis.gov/help/ordermethods.asp?loc=7-4-0#online

GaAs MOEMS Technology

Olga Spahn, Grant Grossetete, Mike Cich, Chris Tigges,
John Reno, Greg Peake, John Klem

Center for Compound Semiconductor Science and Technology
Sandia National Laboratories
P. O. Box 5800
Albuquerque, NM 87185-0603

Abstract

Many MEMS-based components require optical monitoring techniques using optoelectronic devices for converting mechanical position information into useful electronic signals. While the constituent piece-parts of such hybrid opto-MEMS components can be separately optimized, the resulting component performance, size, ruggedness and cost are substantially compromised due to assembly and packaging limitations. GaAs MOEMS offers the possibility of monolithically integrating high-performance optoelectronics with simple mechanical structures built in very low-stress epitaxial layers with a resulting component performance determined only by GaAs microfabrication technology limitations. GaAs MOEMS implicitly integrates the capability for radiation-hardened optical communications into the MEMS sensor or actuator component, a vital step towards rugged integrated autonomous microsystems that sense, act, and communicate.

This project establishes a new foundational technology that monolithically combines GaAs optoelectronics with simple mechanics. Critical process issues addressed include selectivity, electrochemical characteristics, and anisotropy of the release chemistry, and post-release drying and coating processes. Several types of devices incorporating this novel technology are demonstrated.

Contents

I.   Introduction

In the recent past silicon MEMS and MOEMS have undergone a period of explosive growth, both in terms of academic and commercial interest. While silicon has played a dominant role, there is an increasing interest in compound semiconductor approaches. This is driven largely by emerging optical and sensor applications. Optical switching represents one rapidly growing area of MEMS. While silicon approaches abound, including waveguides [1] and tip-tilt mirrors [2], increasingly alternative materials are finding use. In the area of displays, the most successful approach to date utilizes silicon CMOS electronics, but the opto-mechanical element itself is made of aluminum [3]. A number of sensing applications as well as those combining on chip sources and detectors are not possible at all in the silicon material system.

While compound semiconductor materials mechanical properties are not as good as silicon, they are still quite suitable for many micro mechanical applications. Table I illustrates this point by comparing many mechanical properties of silicon and compound semiconductors.

Property	Si	GaAs	InP
Crystal Structure (space group)	Diamond {m3m}	Zinc Blend {$\underline{4}$3m}	Zinc Blend {$\underline{4}$3m}
Lattice constant a, (Å)	5.4311	5.6533	5.8688
Density ρ, (10^3 kg/m^3)	2.329	5.36	4.791
Melting point, T_M (°C)	1413	1238	1740
Specific heat, C_p (J/g K)	0.71	0.327	0.322
Thermal resistivity W, (K cm/W)	0.64	2.27	1.47
Thermal expansion coefficient α_{11}, (10^{-6}/°C)	2.6	6.4	4.56
Debye temperature θ_D (K)	463	370	422
Stiffness Constants (Gpa) c_{11} c_{12} c_{44}	165.6 63.98 79.51	118.8 53.8 59.4	101.1 56.1 45.6
Elastic Compliance Constants (10^{-12} Pa^{-1}) s_{11} s_{12} s_{44}	7.7 -2.1 12.6	11.7 -3.7 16.8	16.38 -5.84 21.93
Fracture Toughness K_{tc}, (MPa m$^{1/2}$)	0.9	0.44	0.36
Hardness, H_{vi} (GPa)	10	7	4.3
Micromechanical Bending Strength Average Value of $\sigma_{f(max)}$ (GPa)	7	2.7	2.2

Table I. Mechanical properties of Si, GaAs and InP [4]

Use of compound semiconductor for realization of MEMS and MOEMS addresses several problems. Because these are usually epitaxially grown, they are monocrystalline,

have atomically flat interfaces and extremely well controlled thickness, unlike polycrystalline materials (such as polysilicon). Also, stress of epitaxial films is much more accurately controllable, (by control of the lattice mismatch) than that of polycrystalline materials (usually controlled by annealing cycles). Most importantly, the right choice of a combination of compound semiconductors, such as GaAs-based or InP-based material system, allows for direct incorporation of optical functions into mechanical structures. This is because compound semiconductors are direct (unlike Si) and have traditionally been used for a variety of active and passive optical elements. Another advantage of compound semiconductors for MEMS/MOEMS applications is the very rich chemistry, which can be used for release of the mechanical layers. There are few material combinations and chemical etches applicable to fabrication of Si MEMS/MOEMS (such as use of SiO2 or BPSG as a sacrificial layer and HF or BOE as chemical etches). In the compound semiconductor arena there are numerous combinations of materials and release etches which can result in MEMS/MOEMS structures. Table II shows several material combinations and possible etch chemistries [5].

Stopping Layer	Sacrificial Layer	Etchant	Selectivity, etch rates[a] (μm/min)	References in [5]
GaAs	$Al_xGa_{1-x}As$ x 0.5 $Al_{0.5}In_{0.5}P$ $In_{0.5}Ga_{0.5}P$ $Al_{0.5}Ga_{0.5}P$	$HF:H_2O$ $HCl:H_2O$ $HCl:H_2O$ $HF:H_2O$	cs[b] , high etch rates cs , high etch rates cs , high etch rates cs , 0.3	[2] [44] [45] [46]
$Al_xGa_{1-x}As$ x 0.4	GaAs	$NH_4OH:H_2O_2$	100,5 (spray)	[47,48]
$Al_{0.3}Ga_{0.7}As$	GaAs GaAs $In_{0.2}Ga_{0.8}As$	Succinic acid: NH_4OH $C_6H_8O_7:H_2O_2: H_2O$ $C_6H_8O_7:H_2O_2: H_2O$	cs 0.2 116, 0.3 121, 0.3	[49] [50] [24]
AlAs	$In_{0.53}Ga_{0.47}As$ $In_{0.53}Al_{0.47}As$	Succinic acid: NH_4OH d:o	1100[c], 0.1 550[c], 0.06	[24]
InP InP	$In_{0.53}Ga_{0.47}As$ $In_{0.53}Al_{0.47}As$ GaAs $Al_{0.3}Ga_{0.7}As$ $In_{0.53}Ga_{0.47}As$	$FeCl_3: H_2O$ $C_6H_8O_7:H_2O_2: H_2O$ $C_6H_8O_7:H_2O_2: H_2O$ $C_6H_8O_7:H_2O_2: H_2O$ $C_6H_8O_7:H_2O_2: H_2O$ $HF:H_2OO_2:H_2O$	cs(?), 0.7 473, 0.2 102, 0.02 960, 0.3 486, 0.2 cs(?),slow etching	[7] [50] [50] [50,51] [50] [4]
$In_{0.53}Ga_{0.47}As$	$In_{0.53}Ga_{0.13}Al_{0.34}As$ $In_{0.53}Al_{0.47}As$ InP	$HCl: H_2O$ $HCl: H_2O$ $HCl: H_2O$	329[c], 0.1 1944[c], 0.6 cs, high etch rate	[52] [52] [12]
InAs	AlSb	HF	cs, high etch rate	[5]
$Al_{0.5}Ga_{0.5}Sb$	InAs GaAs $GaAs_{0.85}Sb_{0.15}$	$C_6H_8O_7:H_2O_2: H_2O$ $C_6H_8O_7:H_2O_2: H_2O$ $C_6H_8O_7:H_2O_2: H_2O$	3850[c], 0.1 13650c, 0.3 3789[c], 0.1	[7] [7] [7]

[a] The etch rates are most often given for the etch rate into the 100 plane, and can only serve as guidance. In some cases the anisotropy may be very large.
[b] Here, "complete selectivity" (cs) means selectivity above 10^6. In these cases, selectivity may, in practice be regarded as complete in nearly all technological applications.
[c] Complete selectivity approached. The measurements were made within this accuracy.

Table II. Sacrificial wet etch systems for selected III-V compound semiconductors [5].

Finally, the zinc blende structure of most common compound semiconductors allows for piezoelectricity as a result of lack of center of symmetry (in contrast to silicon). This property leads to interesting sensing applications

II.   Process issues for GaAs-based MOEMS

Fabrication process for both waveguide and surface normal GaAs-based MOEMS shares certain similarities. Broadly speaking, material to be released must be defined by a dry etch process, then certain areas are protected against release and finally release and drying process take place. Many details are contained in each one of these steps. Figure 1 illustrates these steps schematically:
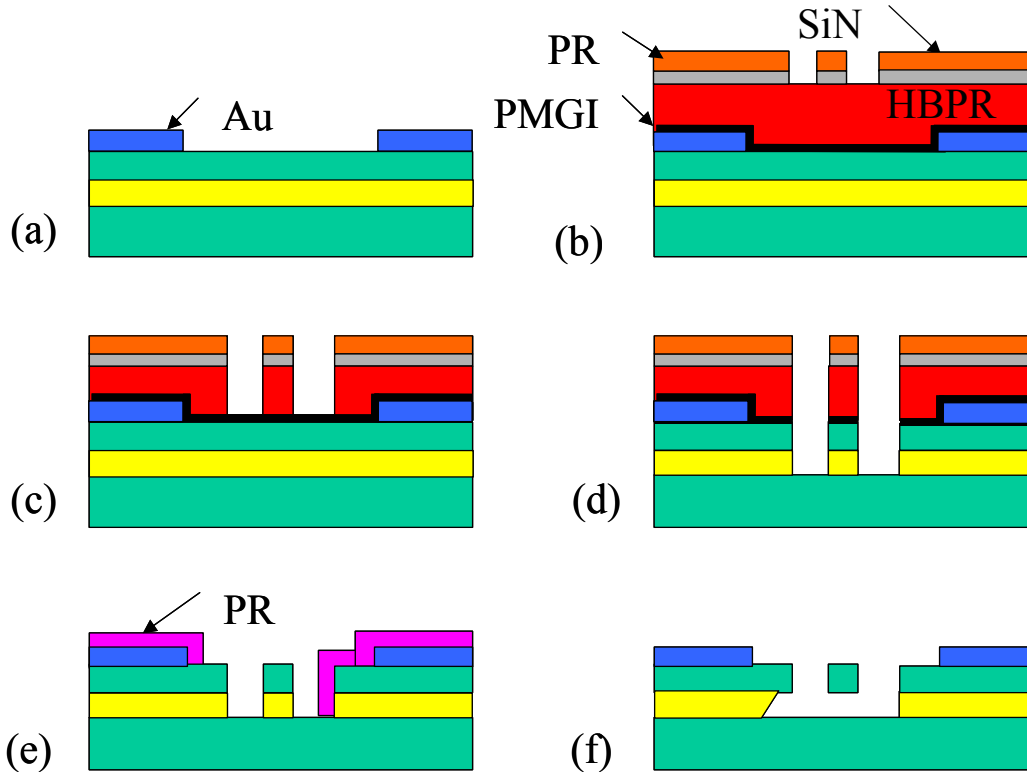

Figure 1 Schematic illustration of the process required for fabrication of the GaAs-based MOEMS. Structural material is indicated in green, whereas the release layer is shown in yellow.

Figure 1a shows deposition of the metal contacts through a lift-off process. In Figure 1b, depositions of the quad-level mask is shown as well as start of the pattern transfer, seen in the top two layers. In Figure 1c, the quad-level mask is fully patterned. In Figure 1d, the quad-level mask pattern is transferred into underlying semiconductor, through the mechanical (green) and sacrificial (yellow) layers. In Figure 1e, the quad-level mask is removed and a protect mask is deposited where we wish to prevent the release of the sacrificial material and finally in Figure 1f, cross section of the fully released and dried sample is shown. Details of this process will be described in the following sections. There are several issues to be contended with during this process. Dry etch process used to transfer the quad-level mask into the semiconductor suffers from micro-loading. That is smaller openings in the mask etch slower then larger open areas. This is illustrated in Figure 2, showing a scanning electron micrograph (SEM) of a cross section of a dry etched GaAs structure. The dark layer is the AlGaAs release layer, which we're trying to etch trough.
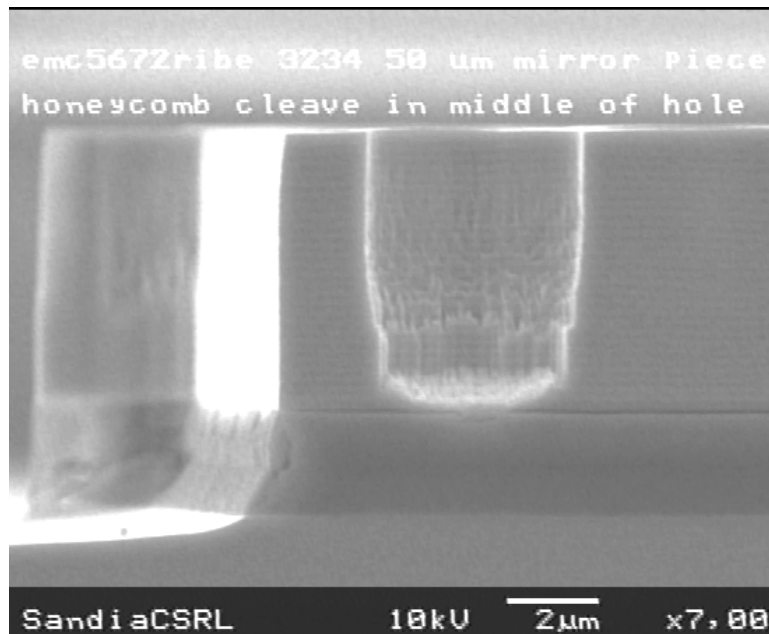

Figure 2 SEM of a cross section of GaAs-based structure showing micro loading effects.

This can be overcome by etching longer, such that the desired depth is obtained in the slower etching small features, whereas the larger features are over-etched. This is problematic; because of mask erosion that causes the lateral feature dimensions to shrink which in turn critically affects mechanical properties such as spring constant. Thus a cantilever waveguide designed to be 3 μm wide on the mask, came out to be 2.4 μm wide upon dry etching. This can be mitigated by compensating in the design of the waveguide for a known over etch factor, however depending on the etch conditions and depth of the etch this factor can vary. Another concern is presented by the somewhat rough sidewall of the etched profile, particularly in the tight spaces. We attempted different methods of etching, such as ICP rather then RIBE, but while smoother sidewalls were obtained the micro-loading problem was worse and we abandoned that method for the semiconductor

dry etch.

Another issues we encountered and solved involved the protect mask. It was crucial to ensure that the protect mask extended well past the edges of the etched structure it was meant to protect (~5 μm) and adhered well to the sidewall and the substrate. If that condition was not satisfied, the release etch seeped underneath the protect mask and undercut the areas meant to be protected. Another factor affecting the effectiveness of the protect mask was the coverage of the etched areas at the foot of the structure. As can be seen in the below figure, the etched corner has a gently sloping feature, in effect a "foot". If that region occurs even partially in the sacrificial layer, upon release the mask lifts up and admits the release etch into areas it is meant to protect. Figure 3 shows a SEM of an adequate and inadequate protect mask coverage and the resultant undercut in the inadequate case.
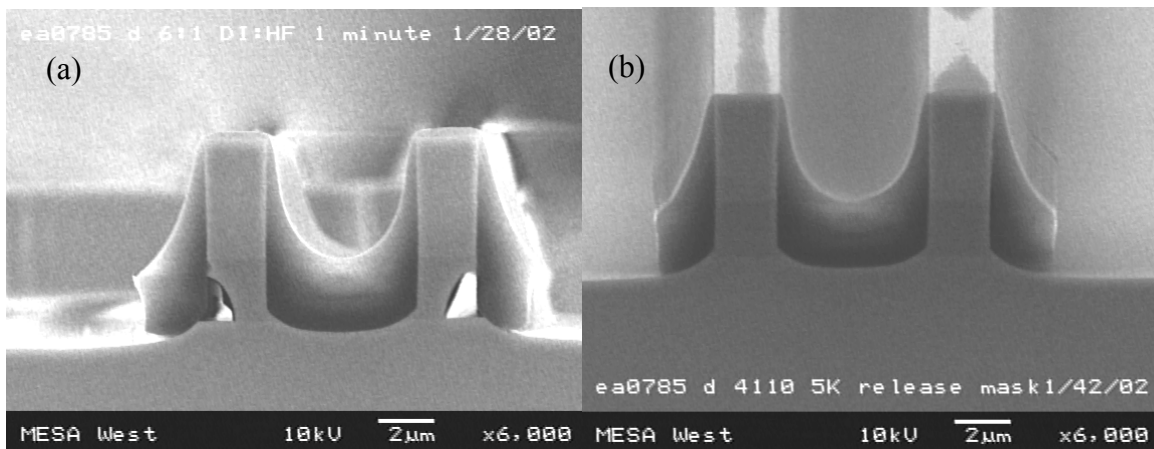

Figure 3 SEMs of protect mask over an etched structure with a) inadequate coverage b) adequate coverage

Another serious issue in processing of the compound devices is the release chemistry. For the majority of this project we concentrated on AlGaAs based sacrificial layers, which are etched with HF solutions. The etch rates accelerate greatly for Al mole fractions greater then 0.5 and are virtually completely selective to GaAs [5]. These structures must then be dried in such a way so as to prevent their collapse due to meniscus forces. This can be accomplished through supercritical drying or sublimation drying. We mostly utilized sublimation drying, although occasionally supercritical drying was used. Occasionally we found surfaces contaminated by scum that would prevent operation of devices or cause stiction if it was sufficiently extensive. While we did not definitively pinpoint the origin of scum, we suspect that RIBE etch contributed to polymerization of the mask on the sidewalls forming a partially organic, partially inorganic polymer that was exceedingly difficult to remove. Figure 4 shows images illustrating this phenomenon. We found that a final bath in a stripper provided by EKC Technology (EKC 922 and EKC 1020) would often improve our results and remove most if not all of the scum.
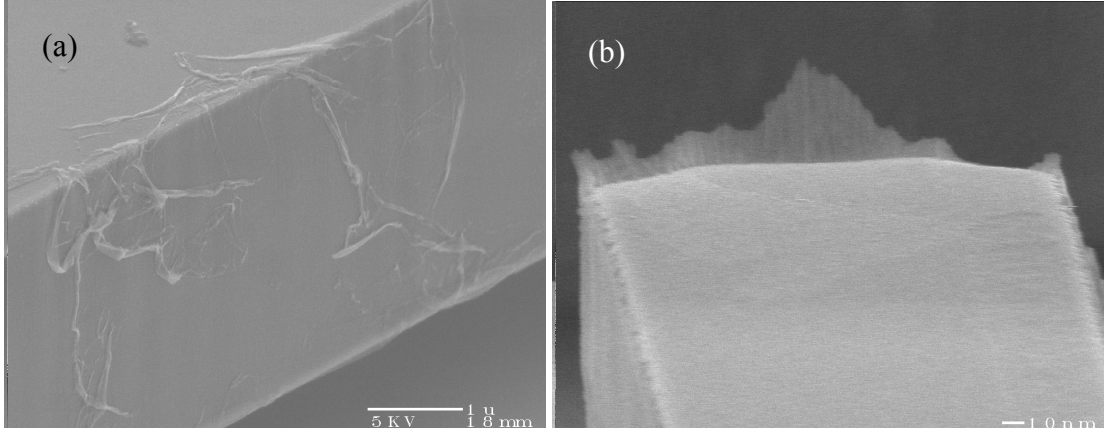
Figure 4 SEMs of scum on the fabricated sample a) sidewall b) sidewall polymer extending above the top edge of the sample.

III. Waveguide Devices

Our work focused on 1xn (where n=2,4 and 8) micro-opto-electro-mechanical (MOEM) switches based on lateral deflection of a planar waveguide. These switches were developed for low-power, wide-bandwidth, high-resolution space-borne array antennas using true-time delay (TTD), but have features which make them attractive for other applications such as dynamic, on-chip signal routing or sensing applications.
The GaAs/AlGaAs switch consists of a deflected cantilever beam with an integrated waveguide and the general concept is illustrated in Figure 5.
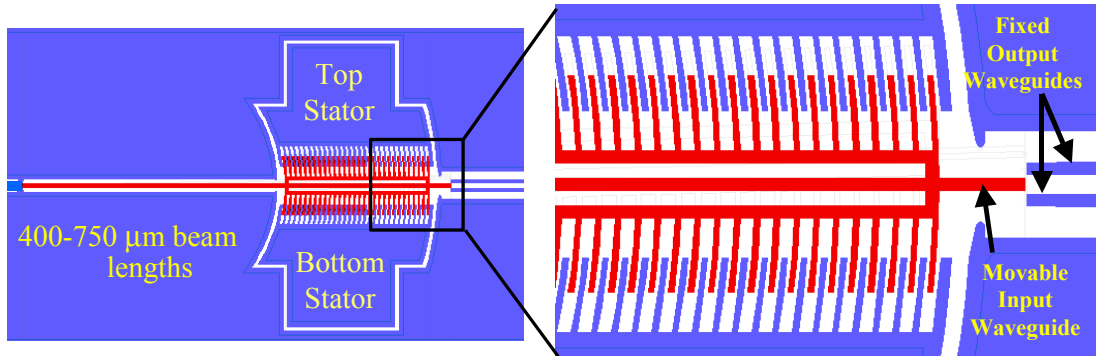

Figure 5 Schematic representation of the waveguide switch; movable parts are marked in red and fixed parts in blue. On the left is the overall view of the switch and on the right is the blow-up view of the movable input waveguide and fixed output waveguide

Actuation is accomplished by electrostatic means, by application of bias between the movable waveguide and static electrodes. This results in 4 µm (12 µm) (28µm) deflection of the 1x2 (1x4) (1x8) cantilevered waveguide in the plane of the wafer, which lines it up with one of the two output waveguides. Layer structure comprising the waveguide and the release layer is shown in Figure 6. Note that the waveguide core is composed of GaAs while the cladding is made up of 4%Al AlGaAs layers. The release layer is a 70% Al AlGaAs layer.
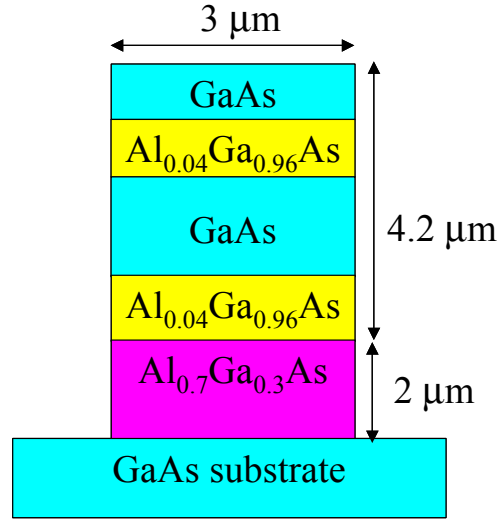
Figure 6 Layer structure of the GaAs MOEMS waveguide

The GaAs/AlGaAs MBE-grown layers are lattice matched to the substrate, resulting in a low stress. This in turn ensures that the released cantilever will remain in plane and the built-in waveguide will line up with the output waveguide upon deflection. Any stress gradients would cause the cantilever to bend vertically, which would cause misalignment to the output waveguides, and therefore reduced performance.

The fabrication of the GaAs MOEMS switch also starts with the formation of ohmic contacts (Figure 1a). The heavily doped n[+]-GaAs contact layer allows the use of e-beam evaporated Ge/Au/Ni/Au for low resistivity ohmic contacts. The metal is structured by lift-off. After contact pads are formed, the mask used to etch the mechanical structure is built. It is a quad-level mask with a 2000Å lift-off layer of PMGI followed by a 1.7 µm layer of AZ4110 photoresist, which is hard-baked at 170°C for one hour. A 3000Å layer of Si_3N_4 is then deposited by PECVD and patterned with a mask of AZ4110 photoresist followed by a CF_4/O_2 plasma etch in a standard parallel plate Reactive Ion Etch (RIE) system. The nitride mask is used as an etch mask for the hard-baked PR which in turn is used as an etch mask for GaAs/AlGaAs.

We have developed two independent processes for subsequent structuring of the hard-baked PR and non-selective etch of GaAs/AlGaAs. In one process the hard-baked PR is etched with O_2/Ar plasma in an ECR-RIE chamber. The etch rate is about 1µm/min and gives highly anisotropic and smooth sidewalls of the hard-baked PR. After structuring the mask, the sample is moved to an Inductively Coupled Plasma Reactive Ion Etch (ICP-RIE) chamber where a mixture of BCl_3, Cl_2 and Ar is used to etch the GaAs/AlGaAs structure. The etch is monitored with an optical interferometer and stopped at the 70%-AlGaAs release layer. The main problem with this process is the severe micro-loading effect in the comb-drive areas, where the etch rate can differ by as much as 50% from the open areas. This makes it hard to maintain good sidewall morphology while ensuring a fully resolved gap between the comb drive fingers.

The second process, and so far the most successful, uses Reactive Ion Beam Etching (RIBE) to structure the hard-baked PR and the GaAs/AlGaAs with a O_2 beam and a Cl_2 beam respectively. The etch rate is much slower than ICP-RIE, but micro-loading is less

of a problem. Using this process we get highly anisotropic and smooth sidewalls. Figure 7 shows a SEM picture of the cantilever beam and the two output waveguides of the switch.
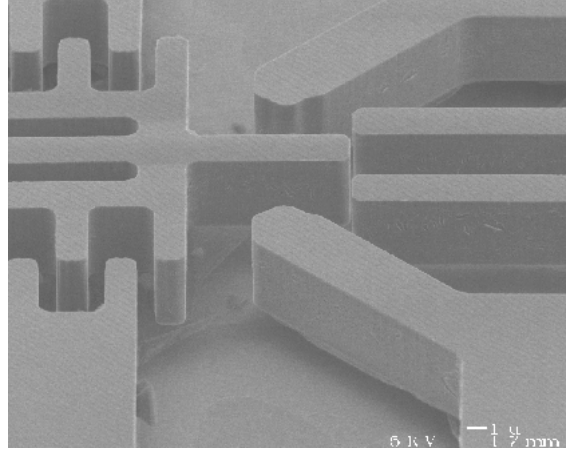

Figure 7 SEM of a cantilevered movable waveguide and two fixed output waveguides

In both cases the sample is soaked in NMP at 90°C for 2 hours, which dissolves the PMGI and lifts off the hard-baked PR. The sample is now ready for release. We use a protection mask of PR only opened up around the cantilever beam structure we want to release. A mixture of 1:3 HF:DI water etches the layer of AlGaAs and undercuts the cantilever beam in about 60 seconds. The sublimation drying process is used as a final step.

Transfer function of the switch was measured by coupling 1.3 µm light from a fiberized YAG laser into the cleaved (and fixed) end of the cantilever waveguide. Upon application of bias to either the top or bottom stator (see Figure 5), the movable cantilever would deflect to line with either one of the fixed output waveguide. We measured the optical power at the end of one of the fixed waveguides as a function of bias applied to the appropriate stator. Figure 8 shows the result. In the figure output power at the fixed output waveguide is shown for a 1x2 switch (dashed lines) and for a 1x4 switch (solid lines), which is also pictured in the inset. For the case of the 1x4 switch, output waveguides A and B are marked in the inset and the maxima in the output power are corresponding to the alignment with waveguides A and B are also marked. Note that Figure 8 shows the characteristic transfer function for deflection in one direction only. Upon application of bias to the other stator a similar characteristic is obtained at the output of the other waveguide. The voltage associated with the peak power measured at the output waveguide is denoted as the actuation voltage and corresponds to the optimal alignment of the cantilever waveguide and the fixed waveguide. This voltage is a function of the spring constant of the cantilever and thus its length. We fabricated and measured devices with cantilever lengths varying from 400 to 750 µm.
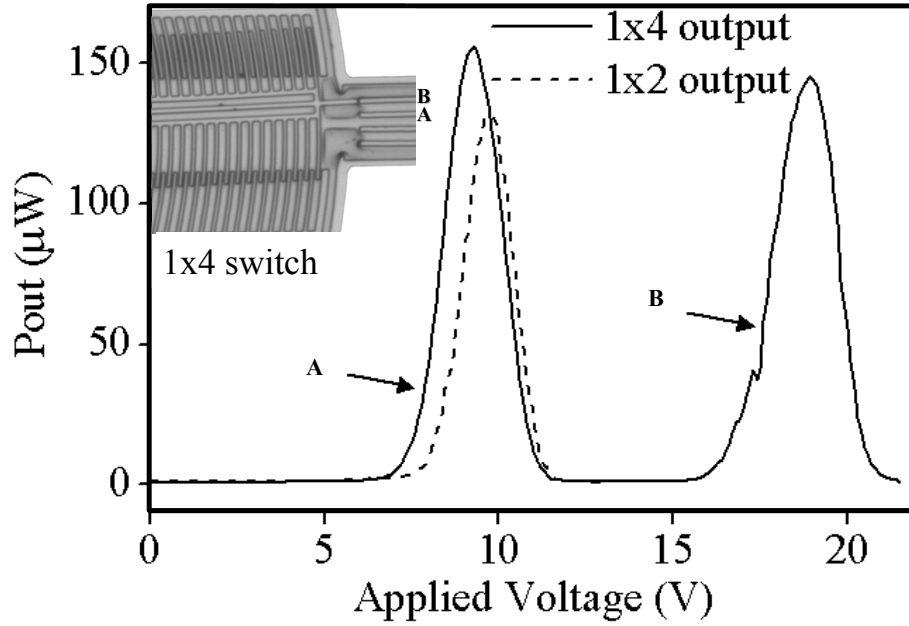
Figure 8 Output power measured at the output of the fixed waveguide as a function of the bias on the appropriate actuator. Dashed lines show output of a 1x2 switch, whereas solid lines show the output of a 1x4 switch. Inset shows a microscope image of the plan view of a 1x4 switch with output waveguides A and B marked

Figure 9 shows the plot of the actuation voltage as a function of the cantilever length (blue curve) as well as resonant frequency as a function of the cantilever length (red curve).
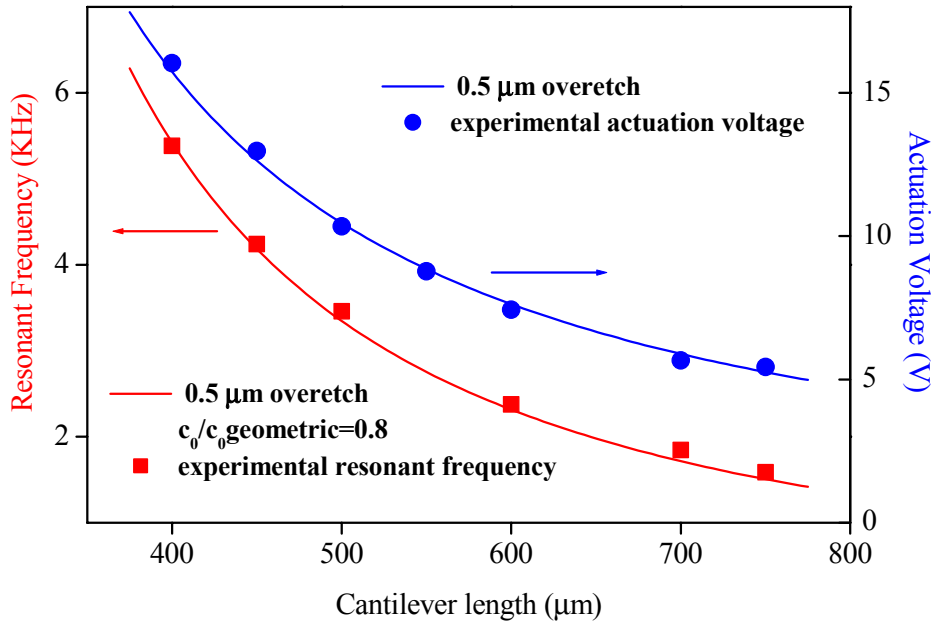

Figure 9 Actuation voltage (blue curve) and the resonant frequency (red curve) as a function of cantilever length

Fit to the experimental points in Figure 9 (shown with blue filled circles) is obtained analytically, assuming a 0.5 μm over-etch on the width of the cantilever. This over-etch is measured from SEM images, using pitch of the waveguide and the comb fingers as a ruler. Analytic fit is indicated with a blue line in Figure 9. Figure 10 shows the theoretical model used in derivation of the fit:
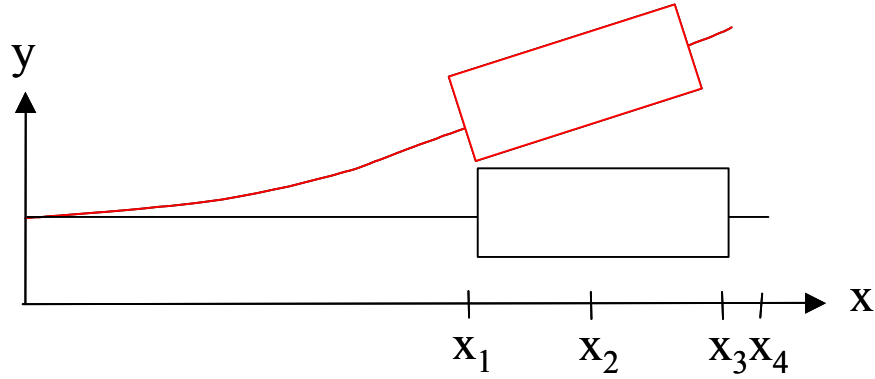

Figure 10 Schematic for the theoretical model of deflection of the cantilever. Black indicates the zero bias position, whereas the red shows the cantilever position upon application of bias.

We assume that all the deflection takes place for $x<x_1$, that is the comb drive and the portion of the waveguide after the comb drive ($x>x_3$) are rigid. Vertical axis y represents deflection in the plane upon actuation. Thus for $x<x_1$ we can represent the cantilever position as:

$$EIy''(x)=F\cdot(x_2-x) \tag{1}$$

Where E is the Young's modulus, I is the moment of inertia, y'' indicates the second derivative of the lateral displacement and F is the applied force. Displacement at the tip can be expressed as and set to 4 μm (displacement distance for complete alignment with the output waveguide):

$$y(x_4)=y'(x_1)x_4+y(x_1)=F/k=4\mu m \tag{2}$$

Where $k=EI/\gamma$ where γ is a geometric function of cantilever length L. Then by setting the restoring force given by Hook's law ($F=kx$) and the electrostatic force given by c_0V^2 where c_0 is the capacitance, the following equation is obtained, from which relationship between V and L can be extracted:

$$V=(EIy(x_4)/\gamma c_0)^{\frac{1}{2}} \tag{3}$$

As seen in Figure 9, we also measured resonant frequency of the cantilevers as a function of the cantilever length (shown with red filled squares). This measurement was obtained in time domain. That is the cantilever was DC biased to a position that allowed 50% of the peak power to be coupled into the output waveguide. Then, a short voltage pulse was

14

applied to set the cantilever into decaying oscillation. Thus, in effect an impulse response was measured, resulting in a measurement like the one shown in Figure 12 below:
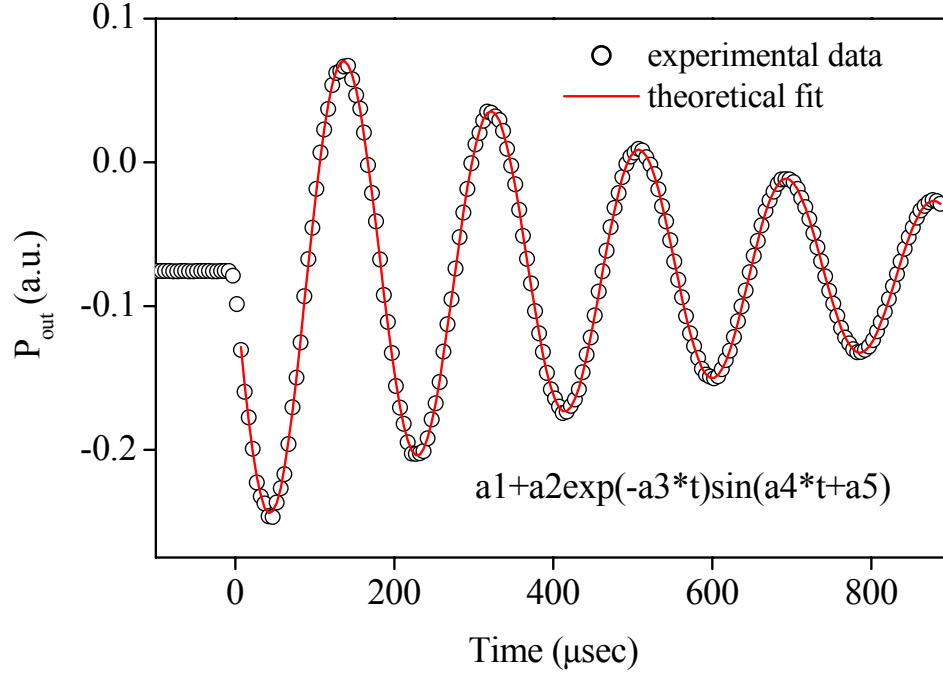

Figure 12 Output power at the end of the fixed waveguide as a function of time. Open black circles indicate data points and the red line is the analytical fit

Data shown in Figure 12 with open black circles was fitted to a following equation (fit is shown with a red line):

$$a_1 + a_2 \exp(-a_3 t)\sin(a_4 t + a_5) \tag{4}$$

Equation (4) is a solution to the following equation of motion that governs the behavior of this system:

$$my'' + \mu y' + ky = 0 \tag{5}$$

Where m is the mass, μ is a variable related to the decay constant and k is a variable related to the spring constant and y indicates the lateral displacement. Resonant frequency is then obtained from the a_4 parameter. It should be noted that the c_0 parameter utilized in these calculation is scaled down to 80% of the geometric value of c_0. This allows for accounting of fringing fields and other electrostatic effects (such as image charges in the substrate).

Further analysis of the dynamics of the system permitted optimization of the drive signals such that the amount of ringing upon switching was minimized and the switching speed was maximized. It should be noted however that the drive voltage influences the switching speed and higher switching speeds can be obtained with higher drive voltage.

Figure 13 a and b shows output power at the end of the fixed waveguide as a function of time when different drive voltage schemes are used:
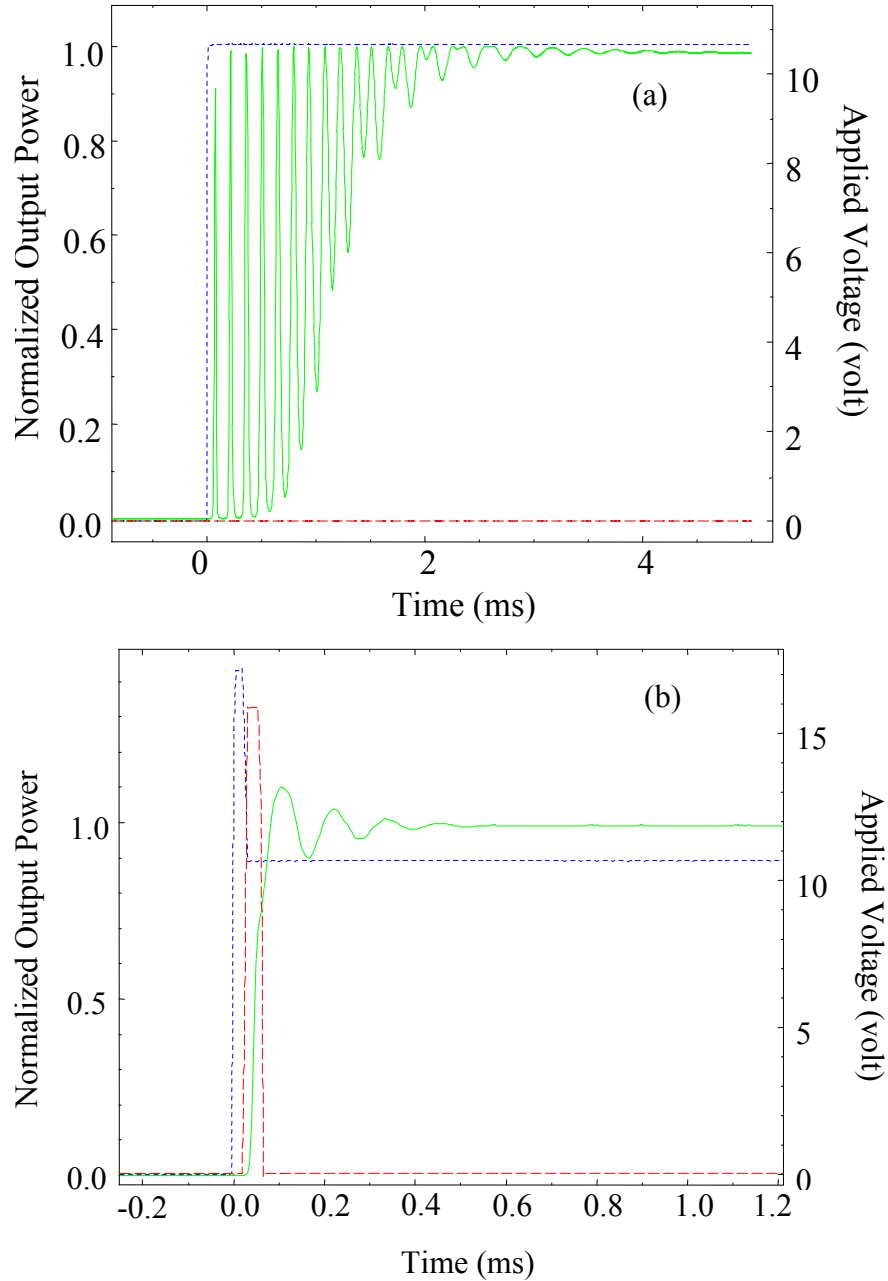

Figure 13 Temporal response of the waveguide (output power at the end of the fixed waveguide – shown in green) with a a) standard square wave voltage applied on the attracting stator (shown in blue dashed line) b) accelerate (shown in blue dashed line) and break pulses (shown in red dashed line) applied on the attracting and breaking stator

In Figure 13 a where a simple square wave voltage is applied to the attracting stator, the response time (time from application of the bias to the first maximum in the response) is 75 μsec, whereas the switch time (time from application of the bias to time when the

response settles) is 4.5 msec. The switching time is rather long due to numerous oscillations. As can be seen from Figure 13 b, where a more complicated drive scheme is employed, the switching time is greatly reduced to 520 μsec and response time is 72 μsec. The reduction in switching time is obtained by application of an accelerating pulse on top of a hold voltage, which is applied, to the stator toward which the cantilever is attracted. At an appropriate delay time, a breaking pulse is applied to the opposite stator. Residual oscillations visible in Figure 13 b are due to out of plane displacement and may be further corrected with application of substrate bias.

IV.   Surface Normal Devices

Another aspect of this work focused on surface normal devices. These devices were designed to demonstrate tip/tilt capability with very high reflectivity. Thus they were referred to as high reflectivity tilt mirrors (HiRTM). There are several applications that demand moderate tip angles (<10°) and very high reflectivities (>98%) such optical time delay for beam forming applications. While there are numerous examples of Si-based devices, this effort represents the first attempt to demonstrate this in a compound semiconductor system. Conceptually, the devices consist of a distributed Bragg reflector (DBR) suspended by two torsional springs. Isolated top electrodes provide a means to attract one edge or the other of the square mirror toward the substrate, resulting in an angular tilt of the mirror. Mirror size and thickness of the sacrificial layer determine the final tilt angle. In our case, we fabricated devices 72 μm and 120 μm on the side with a 2.31 μm thick sacrificial layer. This resulted in a maximum tilt angle of 3.7° and 2.2° for the small and large devices, respectively. The layer stack comprising the mirror is shown in Figure 14. Below, in Figure 15 the basic operation of the tip/tilt mirror is illustrated schematically:
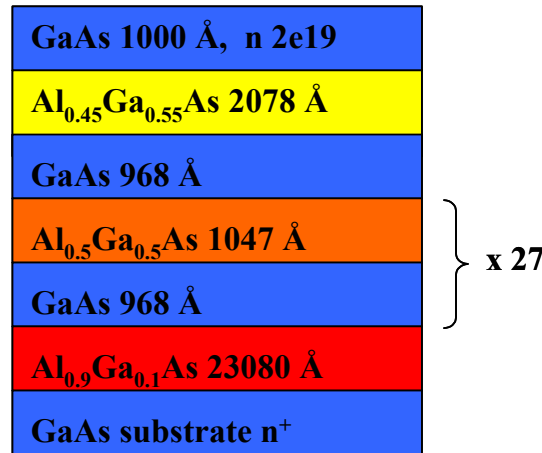

Figure 14 Layer structure of the DBR comprising the tip/tilt mirror

Below, in Figure 15 the basic operation of the tip/tilt mirror is illustrated schematically:
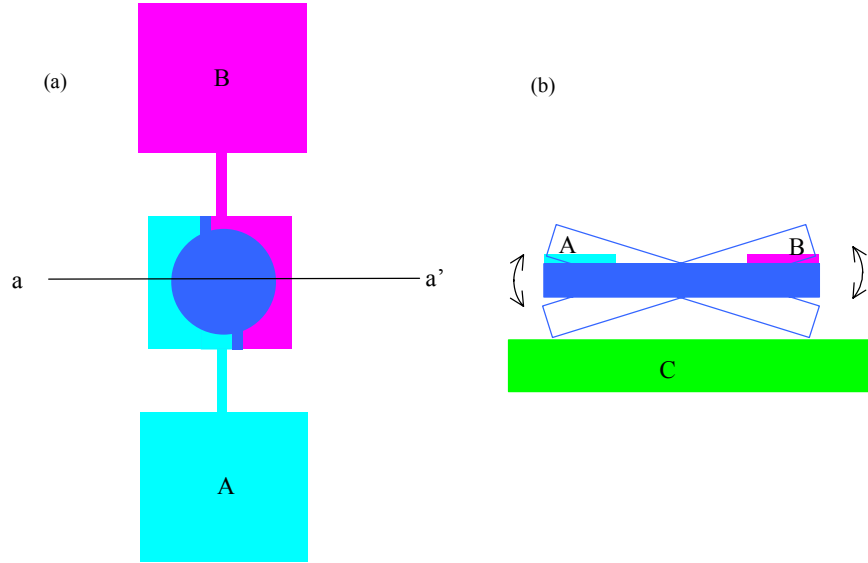
Figure 15 Schematic representation of the mirror operation a) plan view, showing the mirror surface (dark blue) and the contact scheme which connects one side of the mirror to the pad A (turquoise) and the other to the pad B (magenta) b) cross sectional view along aa' of the mirror showing the tilt to the left when bias is applied between pad A and the C (substrate – indicated in green) and to the right when the bias is applied between pad B and the substrate.

Tilt angle obtained by application of bias is sufficiently small, such that reflectivity of the mirror is expected to remain greater then 98% for all tilt angles at 1.32 µm incident wavelength. Figure 16 shows the simulations of the reflectivity for different tilt angles and two different values of the air gap size. It can be seen that for all angles of interest and for the two extrema of the air gap (resonant and anti-resonant) reflectivity at 1.32 µm does not dip below 98%.

Fabrication of the surface normal structure followed a sequence very much like the one for the waveguide device. However, there were several significant differences that affected the fabrication process. At 27.5 periods, the surface normal structure was 5.85 µm thick – 30% thicker then the waveguide structure. This presented unique challenges in the dry etching. Although the sidewall quality was not as crucial as in the waveguide device, presence of 2 µm thick torsional springs mandated that care be taken during the etching process. Due to the size of the mirror to be released (72 µm and 122 µm for small and large mirrors respectively) the undercut distance was much larger then in the waveguide case (36 µm vs. 1.5 µm). To facilitate this we chose our sacrificial region to consist of 90% Al rather then 70% Al as in the waveguide case. This resulted in a faster etch rate for the same HF concentration. However, it was observed that the H bubbles which formed during the etch and became trapped under the mirror or the flexure, broke the thin torsional springs.

27.5 periods of $GaAs/Al_{0.5}Ga_{0.5}As$

$d_{min}=1.5\lambda$

$98.4107< R(1319) <98.43315$

$d_{max}=1.75\lambda$

$99.86185< R(1319) <99.86215$
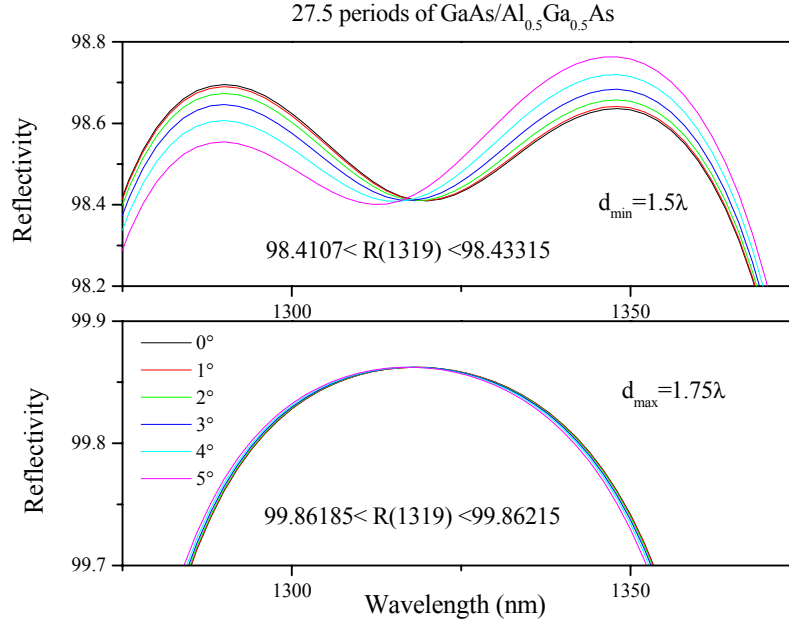
0°
1°
2°
3°
4°
5°

Wavelength (nm)

Figure 16 Simulated reflectivity of the DBR comprising the tip/tilt mirror as a function of wavelength for several different incident angles. Top view shows anti-resonant air gap size ($m\lambda/4$, where m is even) and the bottom shows resonant gap size ($n\lambda/4$, where n is odd).

In order to combat this problem, isopropyl alcohol was added to the etch mixture to reduce the surface tension of the bubbles and break them up before they became large enough to rapture the springs. This approach was successful, however the etch had to be re-calibrated. Thus to successfully release our devices a 17 minute etch consisting of 6:3:1 mixture of DI H_2O:IPA:HF was utilized. This resulted in a complete release of both the large and small mirrors. An additional difficulty was caused by the size of the contact pad, 150 µm x 150 µm. This was too close in size to the mirror, because in order to completely release the mirrors, we undercut the contact pads extensively or they else they floated off altogether.

To combat this, we ordered another mask layer, which would protect the release layer under the contact pad against release. This required that a deeper dry etch, such that the release layer was etched through to the substrate. Thus the total etch depth required now exceeded 8.16 µm, making it very difficult to maintain 2 µm critical feature size. Additionally we found that the etch depth had to be even greater then 8.16 µm, to ensure that the etch "foot" was in the substrate, rather then the release layer. If this condition was not met, the protect photoresist did not adhere well to the sidewalls of the contact pad and protect it against release. Figure 17 illustrates examples of "bad" and "good" protect photoresist coverage.
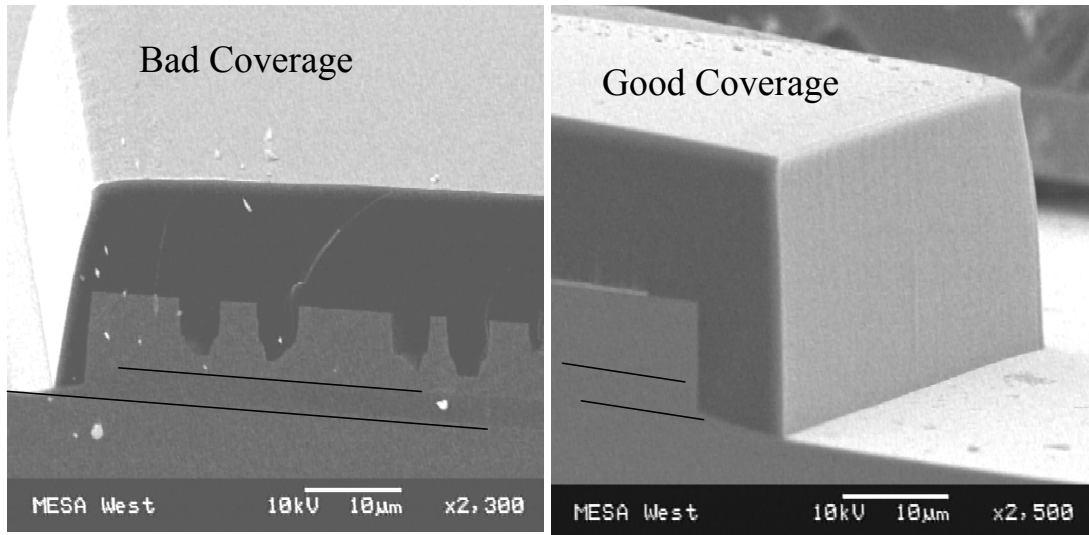
Figure 17 SEM images of the cross section of a HiRTM device with "bad coverage" (left) and "good coverage" (right) of protect photoresist.

Devices with various spring lengths (50 µm to 250 µm in 50 µm increments) were fabricated. Different spring length resulted in a variety of actuation voltages. Shown in Figure 18 below is the tilt angle as a function of voltage for different spring lengths (72 µm mirror).

As expected, longer, more compliant springs actuate at lower voltages, whereas the shortest springs, which are the stiffest, require the highest voltage to actuate. Another interesting effect was observed, in that the mirrors both tilted and moved down in a piston fashion upon actuation. This effect was strongest for the most compliant (i.e. longest
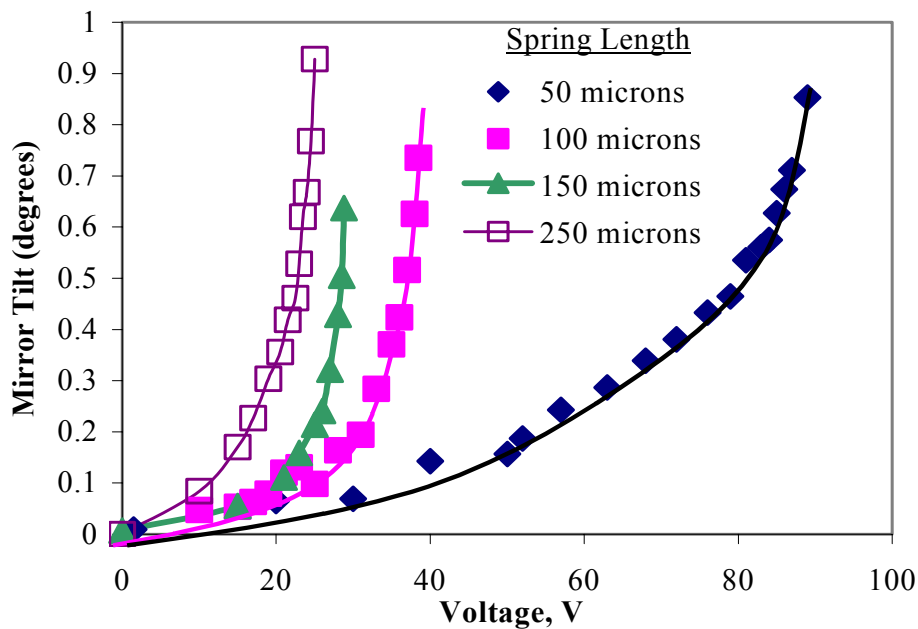

Figure 18 Tilt angle as a function of voltage for different spring lengths

springs). The piston action resulted in a decreased tilt angle (in Figure 18 maximum tilt angle is ~1°, rather then the expected ~3° because the edge of the mirror has not touched the substrate yet. It is also decreased somewhat by the piston action).

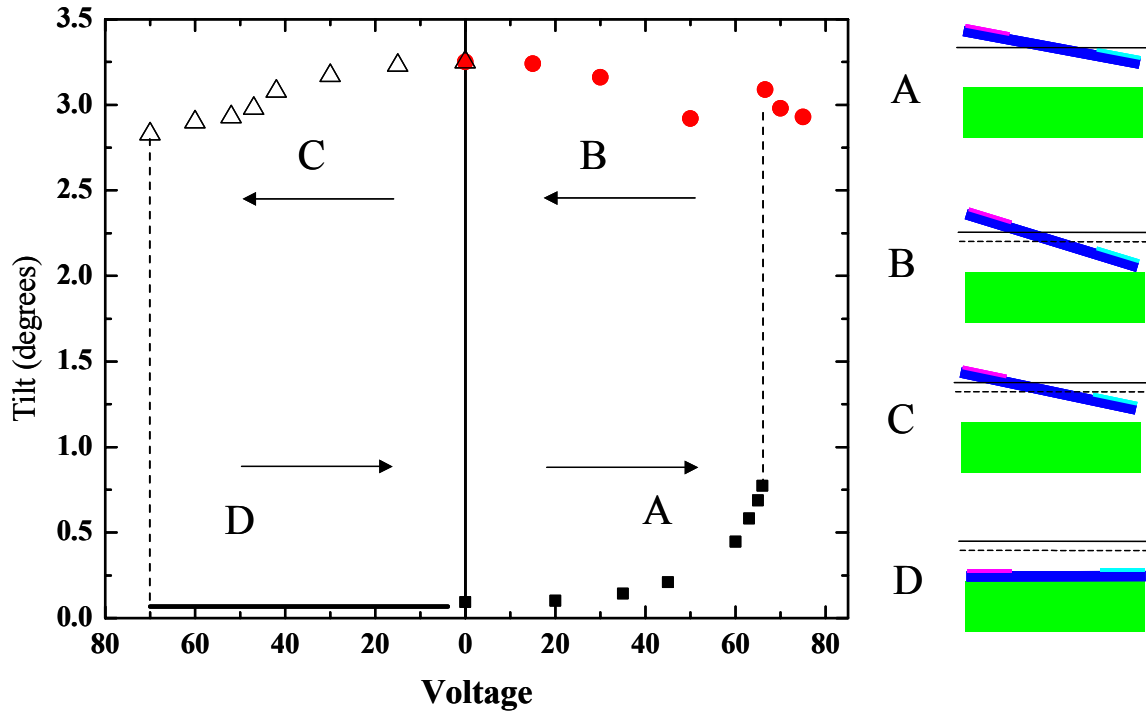Figure 19 Tilt angle as a function of voltage on a 72 μm mirror with a 50 μm spring

This phenomenon results in a peculiar behavior of the mirror as the voltage is applied on one pad and then the other. This is illustrated in Figure 19. First, as the voltage is applied to the right side of the mirror (the turquoise colored pad), the mirror tilts without piston action. This behavior is denoted as the region A and the inset shows schematically what the mirror is doing. This is also the behavior depicted in Figure 18. The arrow is meant to indicate the direction of voltage change (in the region A, it is increasing on the turquoise pad, and floating on the magenta pad). At a certain value of voltage (dependent on the spring length), the mirror sticks down, the edge being actuated to the substrate. This is accompanied by some piston action and results in the maximum angle, which is less then the expected maximum angle by the amount of the piston action. This is shown as the branch B. As the voltage on the turquoise pad is decreased (the direction of the arrow in region B), some piston is removed, while the edge of the mirror is still stuck to the substrate and the angle increases slightly. Curiously, even when all the bias is removed, the mirror edge remains stuck down to the substrate. Next the bias is applied to the other pad ("magenta" in the accompanying schematic on the right). Thus in the region C, the bias is increasing on the opposite (magenta) pad and is floating on the turquoise pad. While the right had side of the mirror is still stuck to the substrate, the left had side is also being lowered toward the substrate, due to the electrostatic attraction. This results in the decrease of angle as seen in the region C. Finally, when sufficient voltage is applied, the entire mirror slaps down to the substrate (region D) and the tilt angle is zero. As the bias

on the magenta pad is lowered (direction of the arrow in region D), the angle remains at zero. It should be noted that the details of this behavior depend highly on the spring constant and the stiction force. In this case a small mirror (72 µm) with a 50 µm spring was tested.

V.   Novel Phenomena

One of the fascinating novel phenomena we observed was the light sensitivity of the MOEMS waveguide switches. It became apparent that the actuation voltage of a given switch was affected by the microscope light, where the presence of the light resulted in a *lower* actuation voltage. To determine whether this was a charge effect caused by the absorption in the waveguide, the devices was illuminated with different wavelength laser light. The results are shown in Figure 20:
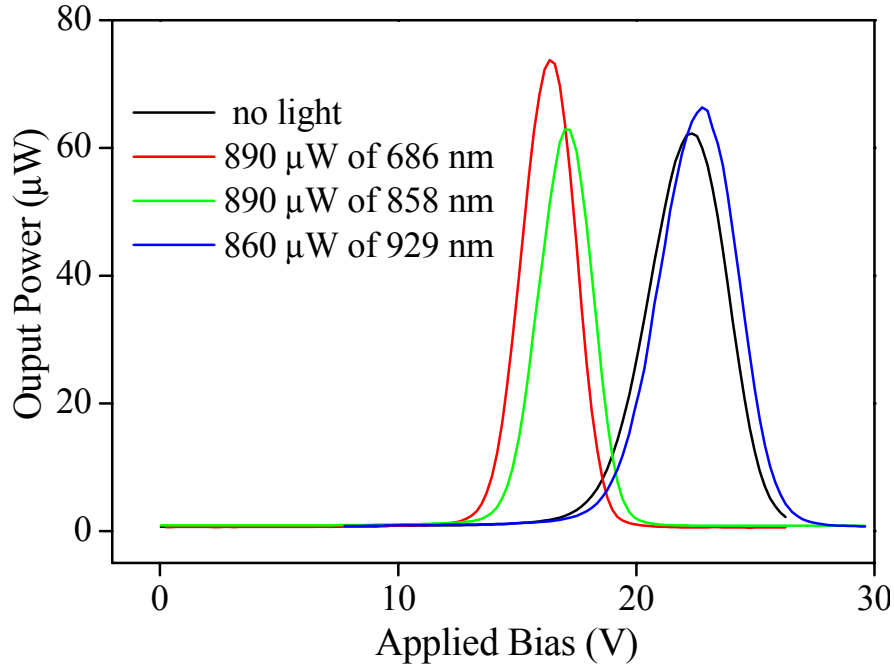

Figure 20 Output power in the fixed waveguide for a 500 µm long cantilever as a function of applied bias. Black curve indicates behavior without top illumination, whereas red, green and blue curves show behavior when the device is top illuminated with 890 µW of 686 nm, 858 nm and 929 nm laser light.

As can be seen above, when the device was top illuminated with laser light of 686 nm and 858 nm the actuation voltage (peak of the curve in Figure 20) was decreased. This is because the band gap of GaAs (the constituent material of the waveguide) is 1.42 eV (or ~870 nm). Thus light of wavelength shorter then band gap is absorbed and carriers are generated, whereas the light of longer wavelength (929 nm) is not absorbed and makes no difference in the actuation voltage.

In order to gain understanding of this phenomenon, a band structure analysis of the waveguide system was performed. Results of the semi-classical simulation of the band edges along the azimuthal direction for this material are shown in shown in Figure 21.
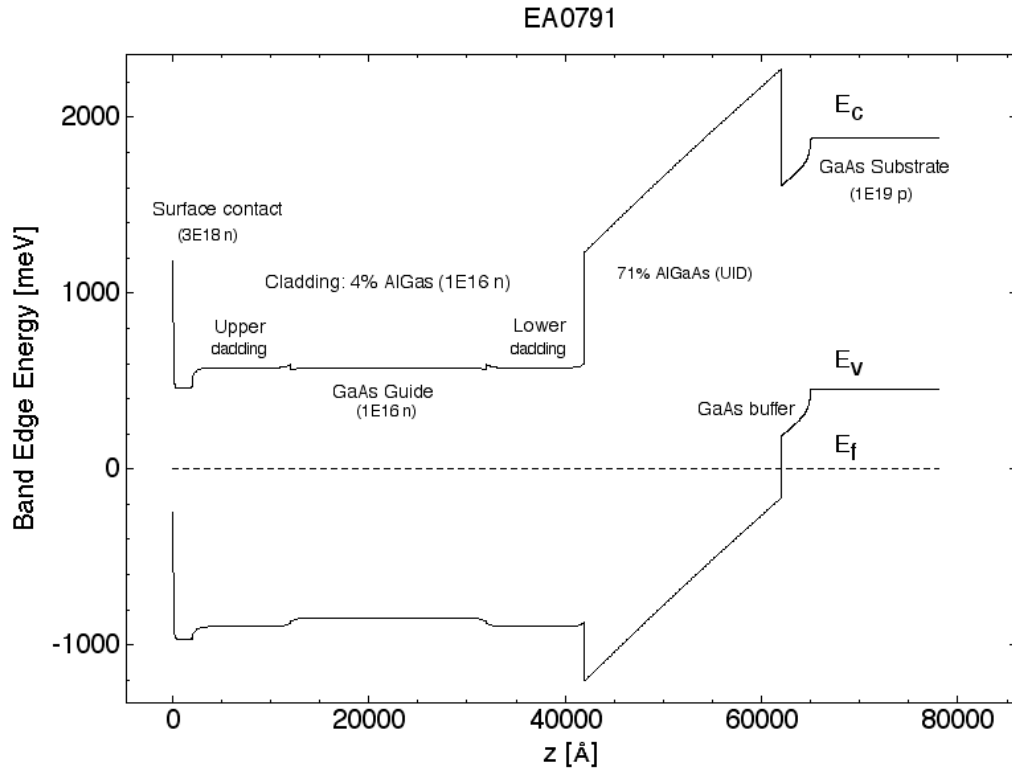

Figure 21. Simulation of the band edges in the material grown for micro-machining an optical wave-guide switch. At the surface is a n-doped GaAs contact 200 nm thick followed by lightly doped 4% AlGaAs claddings and GaAs guide. The substrate is heavily doped p-type. A 71% AlGaAs layer is used for undercutting the wave guide.

Quite apparent is the abrupt drop (Schottky barrier) in the band edges at the surface (z = 0) in the contact layer. The high n-type doping level of $3x10^{18}$ cm^{-3} insures that the material is charge neutral within a relatively short depth from the surface. Closer examination yields a screening length of ~7 nm in this region. The short screening length insures charge neutrality within this layer in just over ~35 nm (charge neutrality is achieved within 5 x of the screening length).

In contrast to the situation in the contact is the situation in the cladding and guide layers. These layers are n-type doped at a level of $1x10^{16}$ cm^{-3} in order to provide a nominal amount of electrical conduction without excessive absorption of light in the wave-guide. At these light doping levels, the screening length of about 120 nm and is considerably longer than the 7 nm for the contact layer. The depth required before charge neutrality is obtained is about 500 nm in these two cases. Noting that a comb tooth has 2 surfaces defining it laterally, only half of a 2 μm wide comb tooth is charge neutral. The consequence of these long screening lengths is that estimates of the tooth capacitance using geometries defined by reference to surfaces only, will be quite inaccurate. Another consequence of light doping is that photo absorption can create free carrier charges

comparable to or exceeding the levels obtained by doping at relatively low intensity. Under these conditions, the screening length can be dramatically shortened and in turn effect the electrostatic coupling through a change in the space charge geometry.

To estimate the effect of light absorption in the cladding and guide layers on the actuator we assume the light intensity is adjusted to a level decreasing the screening length by a factor of 2 and a comb finger gap of 1 μm. Ignoring fringing field effects then the capacitance is increased by about a factor of

$$(x + 4\,\lambda)/(x + 2\,\lambda) \tag{6}$$

Where x is the geometric finger gap and λ is the initial (no light) screening length. Using the suggested values results in about a 20% increase in the actuation force. At high intensities a nearly 50% increase should be expected.

Because the electrical and optical time constants are extremely short relative the characteristic mechanical period, experiments comparing dc light intensity measurements with ac measurements should be sufficient to derive properties of interest for the actuator system, such as inertial mass, spring constant, and capacitance.

A complicating factor in these experiments is the apparent long time constant that might be attributed to charge trapping. Temporal response of a switch biased so that the input is partly coupled to the output wave-guide when light exposure is suddenly applied, held on and then turned off, indicates full recovery is achieved only after an extended period of time exceeding 5 minutes. Thus a full explanation of what is seen cannot be attributed to just the effect of light absorption on the screening length but other effects presumably associated with charge traps (given the long time constants) must also be taken into account. Because the observed long time constant (~ 1 min.) is considerably greater than the natural period of the mechanical system (~ 1 ms), light modulation experiments are not excluded. Quasi-steady state is achieved for times on the order of 1 s, which are sufficiently short to eliminate (or account for) the longer time effects.

Another novel area of inquiry involved alternate release chemistry. In GaAs-based compound semiconductor MEMS, the mechanical release of the moveable structure from the substrate is usually accomplished by the lateral (undercut) etching of a high-aluminum content AlGaAs release layer. The aluminum content of this release layer places a constraint on the composition of other aluminum-containing layers not meant to be etched in the structure. In other words, the selectivity of the etchant system for the different materials present places a limit on the available design parameters.

This is illustrated in Figure 23, which shows comparison between reflectivity of a DBR with 50% (currently used in the HiRTM device) and 90% Al in the low refractive index layer. It should be noted that the mirror with 90% Al low refractive index layer has a much broader stop band, due to increased refractive index contrast. Furthermore, such a mirror achieves a comparable reflectivity with much fewer pairs (15.5) then the mirror with a lower 50% Al AlGaAs low refractive index layer (27.5). This has significant implications for the dry etch required to define the structure.
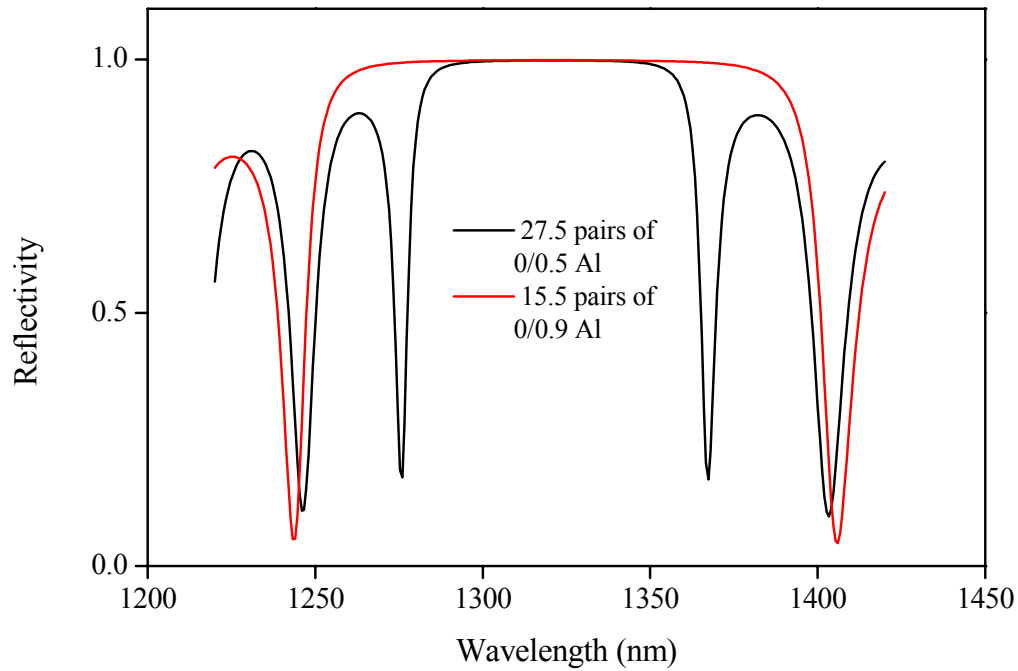
Figure 23 Calculated reflectivity of a DBR with 50% Al AlGaAs low reflective index layer (black curve) and 90% Al AlGaAs low reflective index layer (red curve).

A candidate release material, InGaP, is known to be etched with high selectivity against GaAs using wet chemical etching. While a variety of etch chemistries have been investigated for this material system, there have been no reports of etch undercut rates. In fact, it has been reported in a paper on HBT fabrication that there is no lateral etching of InGaP underneath a GaAs cap layer in HCl [6]. We report the crystallographic dependence of the lateral undercut etch rate of InGaP and show that rapid lateral etching is possible for certain mesa orientations, while other mesa orientations show very small undercut rates.

Sample structures consisting of 0.5 μm of undoped InGaP underneath an undoped 0.5 μm GaAs cap were grown by MOCVD on (100) GaAs substrates cut 2° toward the [110] direction. X-ray diffraction measurements showed the InGaP composition was slightly gallium rich compared to the lattice matched $In_{0.484}Ga_{0.516}P$ to produce a slight (0.55%) coherent lattice strain. Samples were patterned with photoresist to produce an etch test structure consisting of a wagon wheel pattern with 2° spokes and 2° spaces, with a 2 μm width at the center of the structure and 88 μm width at the edge of the wheel. The pattern was aligned to within 0.05° of the cleaved edge of the sample, and the orientation of the pattern with respect to the wafer flats noted. The resist masked a mesa etch through the GaAs cap using 1:8:80 H_2SO_4:H_2O_2:H_2O down to the InGaP layer. The resist was then removed and the sample cleaned in acetone, methanol, isopropyl alcohol, and rinsed in de-ionized water prior to the InGaP etch. The InGaP layer was then etched in unstirred, concentrated (12 M) hydrochloric acid at 20 °C. The etch was stopped by placing the sample in flowing DI for 5 minutes. After etching, the sample was cleaved and the undercut for each mesa measured with a scanning electron microscope (SEM),

accounting for the orientation of the mesa with respect to the cleaved edge. The undercut was defined as the distance between the lower corner of the GaAs cap and the upper corner of the InGaP layer.

Figure 24 shows the etch rate as a function of angle. The etch behavior was found to have twofold rotational symmetry about the [100] axis. Data for mesa orientations more than 180° away from [011] towards [0$\bar{1}$1] has been folded back into the 0-180° zone. Knowing that {111}A planes terminate each etch front, each InGaP surface may be simply modeled as composed of {111}A faces with a step density imposed by the orientation of the mesa. The etch proceeds by step flow – the removal of atoms along these steps. If a mesa edge falls along <011> directions, there are no steps required on the {111} etch front planes and the etch rate decreases to a minimum set by the terrace etching rate. Relative to the step flow etch rate, the terrace etch rate is very slow; measured etch rates for mesas oriented to within 0.05° of <011> are 0.01 µm/min.
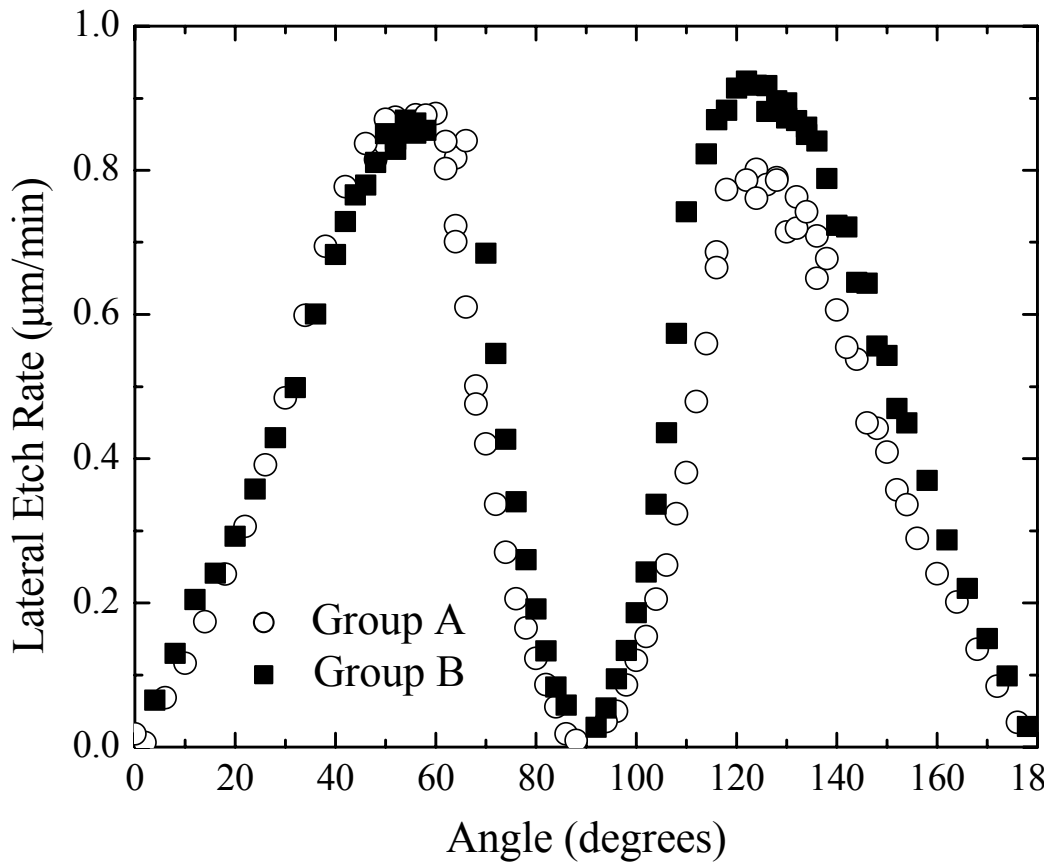

Figure 24 Etch rate of InGaP in HCl as a function of angle of orientation to wafer flat

The data in Figure 24 has been separated into two different sets. Note that this difference is not due to data at angles >180° having a different etch rate. In fact, the etch rate on opposite edges of the same mesa can be seen to be substantially different. This difference

26

can be attributed to the different chemical nature of the steps exposed on these "miscut" surfaces. These different bond configurations will give rise to different kink nucleation rates or kink velocities during etching. On a (111) surface, if a step along $[\bar{1}01]$ is flowing in the $[1\bar{2}1]$ direction, the exposed atom at the edge of the mesa is a triple-bonded phosphorous atom. On the other hand, steps flowing along $[\bar{1}2\bar{1}]$ have a double-bonded phosphorous at the step edge. Therefore the direction of the step flow imposed by the mesa orientation will cause one side of the mesa to etch faster than the other.

However, equivalent steps on the (111) surface lie along $[1\bar{1}0]$. Analysis of the bonding at the step edge in this case produces the opposite expectation for which side of the mesa will etch faster. Therefore a surface reconstruction must stabilize one of these step directions over the other. Without an experiment to determine the orientation of the steps, such as atomic force microscopy on the etched surface, the preferred step orientation on the (111) surface cannot be established. However, the etch data can still be grouped by the flow direction of the steps while recognizing that two different step orientations (e.g. $[1\bar{1}0]$ and $[\bar{1}01]$) can produce step flow in the same average direction (e.g. both $[\bar{1}\bar{1}2]$ and $[1\bar{2}1]$ have a component along $[0\bar{1}1]$). These average step flow directions established by the mesa orientation are used to group the data in Figure 2 as listed in Table 1.

Further evidence of reconstruction is the orientation of the fastest etching mesas. If the only factor determining the etch rate was the step density, the expected orientation of the etch rate maxima will be 45° and 135° from [011] towards $[0\bar{1}1]$, whereas fastest etching is seen at around 55° and 125° from [011] towards $[0\bar{1}1]$. The reconstruction is also evident in the mesa orientation at which the etch front switches from a reentrant slope to a "vee" slope through the mixed front. This transition should also occur at 45° and 135° from [011] towards $[0\bar{1}1]$. Experimentally, the transition is observed away from these directions. For Group A, this transition occurs at 60° and 120°; for Group B the transition orientations are 68° and 112°.

Repeating the experiment with InGaP etch times from 3 to 10 minutes showed that the undercut distance varied linearly with time. Together with the observation of flat, {111}A-defined etched surfaces this shows that the etching rate is chemical-reaction limited. Preliminary experiments using other etchants such as HBr show similar undercut etching behavior. Initial measurements on layers with different InGaP composition (e.g. slightly indium rich compared to $In_{0.484}Ga_{0.516}P$ for a coherent strain of 0.56%) show no strong dependence of the etch behavior on the InGaP composition

VI.   Conclusion

Several novel areas of research were explored under the auspices of this program. A process suitable for fabrication of compound semiconductor based micro-machined devices was developed. Novel waveguide cantilever devices were designed, fabricated and their operation measured and analyzed. Several modeling efforts were undertaken to

understand their performance. Novel optical effects were observed, in effect allowing demonstration of all-optical switching using top illumination, based on interplay of opto-electro-mechanical phenomena. While slow by the standards of electronic switching, such devices offer the possibility of optically triggered, and thus isolated, switching actions.

Furthermore, surface normal HiRTM structures were realized. Unique fabrication challenges associated with their processing were overcome and working devices demonstrated. Bistable switching characteristics were observed, promising a self-latching operation. Preliminary models allowed for understanding of the underlying mechanism. Finally advanced process capabilities were developed, such as use of InGaP as the release material. This capability opens up options in the design area and relaxes some of the dry etch constraints imposed by the geometric factors.

This area is rich in potential new developments in the truly integrated micro-opto-electro-mechanical systems, which could impact many other areas, such as sensing. While an importantly technological foundation has been laid by this program, much more remains to be done.

VII. References

[1] T. T. H. Eng, S. C. Kan, G. K. L. Wong, Sensors and Actuators A 49, 109 (1995)

[2] Hagelin PM, Krishnamoorthy U, Heritage JP, Solgaard O, IEEE Photon. Technol. Lett., 12, 882 (2000)

[3] Van Kessel P.F., Hornbeck L. J, Meier R. E., Couglass M. R., Proc. of the IEEE, 86, 1687 (1998)

[4] Leclercq JL, Ribas RP, Karam JM, Viktorovitch P , Microelectronics Journal, 29, 613 (1998)

[5] Hjort K., J. Micromech. Microeng, **6,** 370 (1996)

[6] M. T. Fresina, Q. J. Hartmann, and G. E. Stillman, IEEE Electron Device Lett. **17**, 555 (1996).

Distribution:

1	MS 9018	Central Technical Files, 8945-1
2	MS 0899	Technical Library, 9616
1	MS 0612	Review & Approval Desk, 9612
1	MS 0188	D. Chavez, LDRD Office, 1030
5	MS 0603	Olga Spahn, 1742
1	MS 0603	Grant Grossetete, 1742
1	MS 0603	Mike Cich, 1742
1	MS 0603	Chris Tigges, 1742
1	MS 0601	John Reno, 1123
1	MS 0601	Greg Peake, 1742
1	MS 0603	John Klem, 1742
1	MS 0603	Chuck Fuller, 1743
1	MS 0601	Tom Bauer, 1123
1	MS 0603	Charles Sullivan, 1742
1	MS 1077	Tom Zipperian, 1740